Calculation of fission observables through event-by-event simulation

Jørgen Randrup[1] and Ramona Vogt[2,3]
[1]*Nuclear Science Division, Lawrence Berkeley National Laboratory, Berkeley, California 94720, USA*
[2]*Physics Division, Lawrence Livermore National Laboratory, Livermore, California 94551, USA*
[3]*Physics Department, University of California at Davis, Davis, California 95616, USA*
(Received 8 June 2009; published 5 August 2009)

The increased interest in more exclusive fission observables has demanded more detailed models. We present here a new computational model, FREYA, that aims to meet this need by producing large samples of complete fission events from which any observable of interest can then be extracted consistently, including arbitrary correlations. The various model assumptions are described and the potential utility of the model is illustrated by means of several novel correlation observables.

DOI: 10.1103/PhysRevC.80.024601 PACS number(s): 25.85.−w, 24.10.−i, 21.60.Ka

I. INTRODUCTION

Nuclear fission presents an interesting and challenging physics problem that is still, about 70 years after its discovery, relatively poorly understood. Although much of the key physics involved is understood qualitatively, a quantitative description is still not in sight, despite vigorous efforts by many researchers.

Because of its inherent complexity, fission provides an important testing ground for both static and dynamical nuclear theories. Furthermore, fission is also important to society at large because of its many practical applications, including energy production and counterproliferation, topics of current urgency.

Whereas the more traditional treatments of fission (see Ref. [1] and references therein) have sought to describe only fairly integral fission properties, such as the average energy release and the average differential neutron yield, many modern applications require more exclusive quantities, such as fluctuations in certain observables (e.g., the neutron multiplicity) and correlations between between different observables (e.g., neutrons and photons). There is thus a need for developing models that include the treatment of fluctuations and correlations.

A potentially powerful approach toward meeting this challenge is to develop simulation models that can generate samples of complete fission events, because a subsequent event-by-event analysis could then provide any specific correlation observable of interest. Furthermore, due to the more detailed quantities that they can address, such models can provide valauble guidance to experimentalists with regard to which observables are most crucial for further progress in the understanding of fission.

Relatively recently, Lemaire *et al.* [2] presented a Monte Carlo simulation of the statistical decay of fission fragments from spontaneous fission of ^{252}Cf and thermal fission of ^{235}U by sequential neutron emission. That work demonstrated how fission event simulations, in conjunction with experimental data on fission neutrons and physics models of fission and neutron emission, can be used to predict the neutron spectrum and to validate and improve the underlying physics models.

We have developed a conceptually similar calculational framework within which large samples of complete fission events can be generated, starting from a fissionable nucleus at a specified excitation energy. The associated computational code is denoted FREYA (fission reaction event yield algorithm). We present here the model in its most basic form that, though quite simplistic in many regards, is already capable of producing interesting results, as we shall illustrate. Furthermore, FREYA was employed in a recent study of sequential neutron emission following neutron-induced fission of ^{240}Pu [3].

In its present early form, FREYA ignores the possibility of neutron emission from the nucleus prior to its fission (*n*th chance fission), and its applications are therefore limited to lower energies, such as thermal fission.

In Secs. II and III we describe how a single fission event is being simulated in the pilot version of FREYA. By repeating the procedure a large number of times, we may generate an entire sample of final fission events, each one consisting of two (slightly excited) residual product nuclei and the various emitted neutron and photons, each one with its associated momentum. In the development of the numerical code, special care has been taken to design the various algorithms for fast execution. As a result, FREYA runs fairly fast, thus making it practical to generate sufficiently large event samples to permit detailed correlation analyzes. In Sec. IV we discuss a number of illustrative results.

II. FISSION

When the possibility of prefission radiation is ignored, the first physics issues concern how the mass and charge of the initial compound nucleus is partitioned among the two fission fragments and how the available energy is divided between the excitation of the two fragments and their relative kinetic energy.

A. Fission-fragment mass and charge distributions

In our current understanding of the fission process, the evolution from the initial compound nucleus to two distinct fission fragments occurs gradually as a result of a dissipative multidimensional evolution of the nuclear shape. However, because no quantitatively reliable theory has yet

been developed for this process, we employ empirical evidence as a basis for selecting the mass and charge partition. Thus, the mass and charge partition of the fissioning nucleus ${}^{A_0}Z_0$ is determined by first selecting the mass partition from a specified probability distribution $P(A_f)$ and subsequently selecting the charge partition from the associated conditional probabibilty distribution $P_{A_f}(Z_f)$.

In a given event, the mass number A_f of one of the fission fragments is selected randomly from a probability density $P(A_f)$ for which we employ five-Gaussian fits to the product mass number distribution [4] shifted upward in mass to ensure a symmetric distribution of the primary fragments,

$$P(A_f) = \sum_{m=-2}^{m=+2} \mathcal{N}_m \mathcal{G}_m(A_f) \tag{1}$$

where each of the five Gaussians has the form

$$\mathcal{G}_m(A_f) = \left(2\pi\sigma_m^2\right)^{-\frac{1}{2}} \mathrm{e}^{-(A_f-\overline{A}_f-D_m)^2/2\sigma_m^2}. \tag{2}$$

Contrary to Ref. [4], we are interested in the primary (i.e., pre-evaporation) fragment distribution rather than the final (postevaporation) product distribution and therefore use $\overline{A}_f = \frac{1}{2}A_0$. The fitted values of the normalizations $\mathcal{N}_m = \mathcal{N}_{-m}$; the displacements $D_m = D_{-m}$; and the dispersions $\sigma_m = \sigma_{-m}$ have some dependence on the excitation energy E_0^*. Because $\sum_A P(A) = 1$ we have $\mathcal{N}_0 + 2\mathcal{N}_1 + 2\mathcal{N}_2 = 1$.

It should be noted that the normalizations $\mathcal{N}_m$ are not quite correct because the sum over the integer fragment mass numbers A_f does not yield the exact integral of the Gaussian and the range of the fragment mass numbers A_f is finite. Because neither of these inaccuracies plays a noticeable role, we shall ignore them in the present preliminary treatment. We also note that merely back-shifting the average $\overline{A}_f$ but not reducing the widths σ_m (to take account of the smearing due to the neutron evaporation) will lead to a product mass distribution that is a bit too wide (because the smearing effect of the neutron evaporation will, in effect, be taken into account twice). However, this effect is rather small and is ignored in the present treatment.

For the subsequent selection of the fragment charge number Z_f, we follow Ref. [2] and employ a normal distribution,

$$P_{A_f}(Z_f) \propto \mathrm{e}^{-(Z_f-\overline{Z}_f)/2\sigma_Z^2} \tag{3}$$

with the condition that $|Z_f - \overline{Z}_f| \leqslant 5\sigma_Z$. The centroid is determined by demand that the fragments have the same charge-to-mass ratio as the fissioning nucleus, on average, $\overline{Z}_f = A_f Z_0/A_0$. We use the values of the dispersion σ_Z measured by Reisdorf *et al.* [5], 0.40 for ${}^{236}\mathrm{U}(n, f)$ and 0.50 for ${}^{239}\mathrm{Pu}(n, f)$. [There appears to be an error (presumably typographical) in the expression (2) for $P(Z)$ in Ref. [2]: the pre-exponential factor should be a square root for $P(Z)$ to be normalized to unity.]

B. Scission energetics

We obtain the fission energetics by assuming that the two fission fragments lose contact at a certain scission configuration that we take to be two coaxial spheroidal prefragments with a specified tip separation d. For the time being, we ignore the nuclear proximity attraction between the two prefragments as well as any possible relative motion at the time of scission. These two effects, which counteract one another, are relatively small but should ultimately be considered.

We introduce some degree of distortion of the prefragments relative to their ground-state shapes, due to their mutual Coulomb repulsion. This is done primarily to ensure that the resulting fragment excitations (and hence the neutron multiplicities) roughly resemble those observed. Thus, generally, the deformation of the fragment at scission, $\varepsilon_{\mathrm{sc}}$, is larger than that of the ground state, $\varepsilon_{\mathrm{gs}}$. The associated distortion energy is calculated by using the small-deformation approximation [6], $\delta V = \frac{8}{45}[E_S^0 - \frac{1}{2}E_C^0](\varepsilon_{\mathrm{sc}}^2 - \varepsilon_{\mathrm{gs}}^2)$, which suffices at this early stage of the development. (Here we use the macroscopic expressions for the surface energy E_S^0 and the Coulomb energy E_C^0 for the spherical shape, as described in Appendix A.) The distortion moves the prefragment centers apart, for any fixed tip separation d, and thus lowers the mutual Coulomb repulsion V_{ij}^C.

It follows that there are two contributions to the total excitation of each prefragment,

$$E_i^* = \delta V_i + Q_i, \tag{4}$$

namely the distortion energy δV_i and the statistical excitaiton (heat) Q_i.

The Coulomb repulsion between the two deformed prefragments is calculated by means of the formula derived in Ref. [7] for two coaxial, uniformly charged spheroids,

$$V_{ij}^C = e^2 \frac{Z_i Z_j}{c_i + c_j + d} F(x_i, x_j). \tag{5}$$

The factor F is unity for two spheres and larger if one or both fragments are prolate. It depends on the dimensionless deformation measures x_i given by $x_i^2 = (c_i^2 - b_i^2)/R_i^2$, where $c_i = R_i[1 + \frac{1}{3}\varepsilon]/[1 - \frac{2}{3}\varepsilon]^{2/3}$ is the major axis and $b_i = R_i[1 - \frac{2}{3}\varepsilon]/[1 + \frac{1}{3}\varepsilon]^{1/3}$ is the minor axis, while R_i is the average radius of the fragment.

Once the fragments have lost contact, they are accelerated by their mutual Coulomb repulsion and their shapes relax to their equilibrium forms. The scission distortion energies are converted into additional statistical excitations of the respective fragments. We assume that these processes have been completed before the de-excitation processes begin.

With the (significant) simplifications described above, we have the following simple energy relations for any particular fission channel, ${}^{A_0}Z_0 \rightarrow {}^{A_L}Z_L + {}^{A_H}Z_H$,

$$\begin{aligned} M_0^* &= M_0^{\mathrm{gs}} + E_0^* = M_L^{\mathrm{gs}} + E_L^* + M_H^{\mathrm{gs}} + E_H^* + V_{LH}^C \\ &= M_L^* + M_H^* + K_{LH}. \end{aligned} \tag{6}$$

Here M_i^{gs} is the ground-state mass of the nucleus ${}^{A_i}Z_i$, $i = 0, L, H$, and E_i^* is its excitation, so $M_i^* = M_i^{\mathrm{gs}} + E_i^*$ is its total mass. [The ground-state masses are taken from the compilation by Audi *et al.* [8], supplemented by calculated masses by Möller *et al.* [9] where no data are available.] Furthermore, V_{LH}^C is the Coulomb repulsion between the two light and heavy fragments at scission. This energy is, by *fiat*, fully converted into relative kinetic energy of the two

receding fission fragments, K_{LH}. Thus, in addition to ignoring any possible postscission dissipation, we also disregard any angular-momentum effects. While these effects are expected to be small, it might be of interest to include them at a later time. The Q value associated with the particular fission channel is given by

$$Q_{0\to LH} = M_0^{\rm gs} + E_0^* - M_L^{\rm gs} - M_H^{\rm gs} = K_{LH} + E_L^* + E_H^*. \tag{7}$$

C. Thermal fluctuations

Once the scission configuration is known, its average total internal (statistical) excitation energy, $\overline{Q}$, can be readily obtained,

$$\overline{Q} \equiv \overline{Q}_L + \overline{Q}_H = M_0^{\rm gs} + E_0^* - M_L^{\rm sc} - M_H^{\rm sc} - V_{LH}^C, \tag{8}$$

where $M_i^{\rm sc} = M_i^{\rm gs} + \delta V_i$ is the mass of the distorted prefragment of the scission configuration. We assume that this internal energy $\overline{Q}$ is partitioned statistically between the two prefragments, as would be the case when the two are in mutual thermal equilibrium. Thus, on the average, the total excitation energy is divided in proportion to the respective heat capacities. These in turn are characterized by the Fermi-gas level-density parameters a_i that are approximately proportional to the fragment masses A_i; we use the values calculated in Ref. [10] (see Appendix B). [We note that those calculations were made for nuclei in their ground-state shapes, whereas the scission prefragments are distorted and may thus have different effective level-density parameters.] The mean excitation in a nucleus is assumed to be $\overline{Q}_i = a_i T_i^2$, so the heat capacity is $\partial \overline{Q}_i/\partial T_i = 2a_i T_i \propto a_i$. Because the two prefragments in the scission configuration have a common temperature, $T_{LH} = [\overline{Q}/(a_L + a_H)]^{1/2} = [\overline{Q}_i/a_i]^{1/2}$, we use $\overline{Q}_i = a_i T_{LH}^2$.

The fluctuations in the statistical excitation Q_i are given by the associated thermal variances, $\sigma_i^2 = 2\overline{Q}_i T_{LH}$. The fluctuations δQ_i are therefore sampled from normal distributions with variances σ_i^2. The prefragment excitations in a given event are then $Q_i = \overline{Q}_i + \delta Q_i$.

As a result of the fluctuations in the statistical excitation energies of the individual prefragments, Q_i, the combined statistical excitation energy, $Q = Q_L + Q_H$, will also fluctuate. This fluctuation in turn implies a compensating fluctuation in the total fragment kinetic energy, so that $K_{LH} = \overline{K}_{LH} + \delta K_{LH}$ where

$$\overline{K}_{LH} = V_{LH}^C, \quad \delta K_{LH} = -\delta Q_L - \delta Q_H. \tag{9}$$

We note that the resulting thermal distribution of heat in each prefragment is approximately Gaussian,

$$P_i(Q_i) \approx \left(2\pi\sigma_i^2\right)^{-\frac{1}{2}} {\rm e}^{-(Q_i-\overline{Q}_i)^2/2\sigma_i^2}. \tag{10}$$

Consequently, the distribution of the combined amount of heat in both fragments, $Q = Q_L + Q_H$, is also approximately Gaussian and the associated variance is the sum of the individual variances, $\sigma_Q^2 = \sigma_L^2 + \sigma_H^2$. Energy conservation implies that the distribution of the total kinetic energy K_{LH} is a Gaussian with the same width, $\sigma_K = \sigma_Q$, as was assumed in Ref. [2].

It is physically reasonable that the partioning of the total energy between kinetic energy and internal excitation fluctuates because the evolution of the fissioning system from saddle to scission is a dissipative process. The associated conversion of the collective energy to heat is the result of many elementary stochastic processes. The fluctuation-dissipation theorem then relates the average energy loss (the dissipation) to the associated fluctuation. Energy conservation demands that the fluctuations in the kinetic energy are exactly the opposite of those in the internal excitation. These, in turn, are given by the above thermal expressions insofar as statistical equilibrium is maintained during the shape evolution from saddle to scission. [We ignore the possibility that the scission configuration itself might also fluctuate from one event to another for a given fission channel.]

Once the relative kinetic energy K_{LH} has been obtained as described above, the magnitude of the relative momentum, p_{LH}, of the fully accelerated fragments is then determined. Because the kinetic energy is relatively small ($K_{LH} \approx 200$ MeV, while $M_0^* > 200$ GeV), we may safely assume that $K_{LH} \ll M_i^*$ and use nonrelativistic kinematics, $p_{LH}^2 = 2\mu_{LH} K_{LH}$, where the reduced fragment mass is $\mu_{LH} = M_L^* M_H^*/(M_L^* + M_H^*)$ with $M_i^* = M_i^{\rm sc} + Q_i = M_i^{\rm gs} + \delta V_i + Q_i$ being the total mass of the excited prefragment. Ignoring any angular momentum effects, we select the fission direction $\hat{\boldsymbol{V}}$ randomly. The fragment momenta are then $\boldsymbol{P}_L = p_{LH}\hat{\boldsymbol{V}}$ and $\boldsymbol{P}_H = -p_{LH}\hat{\boldsymbol{V}}$, in the frame of the fissioning nucleus.

III. POSTFISSION RADIATION

As mentioned above, we assume that the two excited fragments do not begin to de-excite until after they have been fully accelerated by their mutual Coulomb replusion and their shapes have reverted to their equilibrium form, which we take to be those of their ground states. [In principle, the equilibrium shape of a nucleus depends on its excitation because both shell effects and surface tension are temperature dependent, but we have ignored this relatively minor complication at this time.] Furthermore, we ignore the possibility of charged-particle emission from the fission fragments.

Each of the fully relaxed and accelerated fission fragments typically emits one or more neutrons as well as a (larger) number of photons. We assume that neutron evaporation has been completed (i.e., no further neutron emission is energetically possible) before photon emission sets in. This simplifying assumption obviates the need for knowing the ratio of the widths, $\Gamma_\gamma(E_i^*)/\,\Gamma_n(E_i^*)$.

A. Statistical evaporation of neutrons

We treat postfission neutron radiation by iterating a simple treatment of single neutron evaporation until no further neutron emission is energetically possible.

Statistical neutron evaporation is but one example of a general two-body decay. In the present case, the initial body is an excited nucleus with a total mass equal to its ground-state mass plus its excitation energy, $M_i^* = M_i^{\rm gs} + E_i^*$. The Q value for neutron emission is then $Q_{\rm n} = M_i^* - M_f^{\rm gs} - m_{\rm n}$,

where $M_f^{\rm gs}$ is the ground-state mass of the daughter nucleus and $m_{\rm n}$ is the mass of the (unexcitable) ejectile (the neutron). The Q value equals the maximum possible excitation energy of the daughter nucleus, which is achieved for vanishing final relative kinetic energy, $Q_{\rm n} = E_f^{\rm max}$, which would be obtained if the emitted neutron had no kinetic energy. It is related to the associated maximum daughter temperature $T_f^{\rm max}$ by $a_f(T_f^{\rm max})^2 = E_f^{\rm max}$, where a_f is the level-density parameter of the daughter nucleus (see Appendix B).

1. Spectral profile

Once the Q value is known, it is straightforward to sample the kinetic energy of an evaporated neutron, assuming that it is isotropic in the rest frame of the emitting nucleus. We first note that the kinetic energy of the neutron has the form $\epsilon_{\rm n} = p_{\rm n}^2/2m_{\rm n}$ while $v_{\rm n} \propto \sqrt{\epsilon_{\rm n}}$ (nonrelativistically) so that $d^3\boldsymbol{p}_{\rm n} \propto \sqrt{\epsilon_{\rm n}}d\epsilon_{\rm n}$ for isotropic emission. The differential distribution is then [11,12]

$$\frac{d^3\nu}{d^3\boldsymbol{p}_{\rm n}}\,d^3\boldsymbol{p}_{\rm n} \propto \sqrt{\epsilon_{\rm n}}\,{\rm e}^{-\epsilon_{\rm n}/T_f^{\rm max}}\sqrt{\epsilon_{\rm n}}d\epsilon_{\rm n}\,d\Omega = \epsilon_{\rm n}\,{\rm e}^{-\epsilon_{\rm n}/T_f^{\rm max}}d\epsilon_{\rm n}\,d\Omega \tag{11}$$

in the rest frame of the emitting nucleus. The form $\sqrt{\epsilon_{\rm n}}\exp(-\epsilon_{\rm n}/T)$ can be understood as the product of the thermal occupancy of the neutron, $\propto \exp(-\epsilon_{\rm n}/T)$, and its normal speed $v_{\rm n} \propto \sqrt{\epsilon}_{\rm n}$ that introduces a bias in favor of those neutrons that are moving perpendicular to the nuclear surface.

The kinetic energy of the evaporated neutron, $\epsilon_{\rm n}$, is sampled by means of a specific fast algorithm that is described in Appendix C. We note that the form of the energy spectrum implies that the evaporated neutron has a mean (relative) kinetic energy of $\langle\epsilon_{\rm n}\rangle = 2T_f^{\rm max}$ and an associated variance of $2(T_f^{\rm max})^2$. These expressions apply to the particular stage of the evaporation chain. Generally, the first neutron evaporated from the fragment will tend to have a higher energy than the second one and so on.

2. Kinematics

Although relativistic effects are very small, we wish to take them into account to ensure exact conservation of energy and momentum, which is convenient for code verification purposes. We therefore take the above sample value ϵ to represent the *total* kinetic energy in the rest frame of the mother nucleus, i.e., it is the kinetic energy of the emitted neutron *plus* the recoil energy of the residual daughter nucleus. The excitation energy in the daughter nucleus is then given by

$$E_f^* = Q_{\rm n} - \epsilon_{\rm n}. \tag{12}$$

Because the relativistic mass of the daughter nucleus is $M_f^* = M_f^{\rm gs} + E_f^*$, it is possible to calculate the momenta of the emitted neutron and the excited daughter as follows.

Generally, if a particle of mass M decays into two particles of masses m_1 and m_2, those two particles are emitted back-to-back in the rest frame of the initial particle, with their momenta having equal magnitudes. Denoting this common momentum magnitude by p, application of elementary energy conservation yields

$$M = E_1 + E_2 = \left[m_1^2 + p^2\right]^{1/2} + \left[m_2^2 + p^2\right]^{1/2} \tag{13}$$

from which the magnitude p can be readily obtained,

$$4M^2p^2 = \left[M^2 - (m_1 + m_2)^2\right]\left[M^2 - (m_1 - m_2)^2\right]. \tag{14}$$

The individual energies, $E_i = [p^2 + m_i^2]^{1/2}$, may then be obtained subsequently. We employ the above formula with $M = M_i^*$, $m_1 = m_{\rm n}$, and $m_2 = M_f^* = M_f^{\rm gs} + Q_{\rm n} - \epsilon_{\rm n}$.

Assuming that the emission is isotropic (which follows from the neglect of angular-momentum effects), we may readily sample the direction of relative motion (ϑ, φ). The momentum of the ejectile is then

$$\boldsymbol{p}_{\rm n} = (p\,\cos\varphi\,\sin\vartheta,\, p\,\sin\varphi\,\sin\vartheta,\, p\,\cos\vartheta), \tag{15}$$

while the recoil momentum of the residue is the opposite, $\boldsymbol{P}_f = -\boldsymbol{p}_{\rm n}$. These momenta are in the two-body center-of-mass frame, the frame of the mother nucleus, which would generally be moving. We therefore need to boost these momenta to the overall reference frame (see Appendix D).

The emission procedure described above may be repeated until no further neutron emission is energetically possible. That happens when $E_f^* < S_{\rm n}$, where $S_{\rm n}$ is the neutron separation energy for the daughter nucleus, $S_{\rm n} = M(^AZ) - M(^{A-1}Z) - m_{\rm n}$.

B. Statistical emission of photons

Although, at this initial stage, our main focus is on neutron evaporation, we wish to also include an approximate treatment of photon emission. For this purpose we disregard nuclear structure effects and treat the postevaporation photon cascade in a manner that is similar to the neutron emission described above. Clearly, this part can be refined by taking account of the specific level structure in the fission fragments. Because the photon is massless, we introduce an energy cutoff (see below).

Furthermore, the vanishing photon mass causes it to be ultrarelativistic with $p_\gamma c = \epsilon_\gamma$ and $v_\gamma = c$. Consequently,

$$\frac{d^3N_\gamma}{d^3\boldsymbol{p}_\gamma}\,d^3\boldsymbol{p}_\gamma \propto \epsilon_\gamma^2{\rm e}^{-\epsilon_\gamma/T_f}d\epsilon_\gamma\,d\Omega \tag{16}$$

as was also used in Ref. [13]. For the first photon to be emitted, T_f is the temperature in the nucleus right after the last neutron was evaporated, $a_fT_f^2 = E_f^*$, and generally it is the temperature *before* the next photon is emitted.

The photon energy ϵ_γ is sampled by a fast algorithm (see Appendix C) and the nuclear excitation energy is reduced correspondingly, $(E_f^*)' = E_f^* - \epsilon_\gamma$. The spectral shape (16) yields an average photon energy of $\langle\epsilon_\gamma\rangle = 3T_f$ and an associated variance of $3T_f^2$ for a fixed value of T_f. Because, in principle, the continuous form of the spectrum leads to an infinite number of ever softer photons, we keep track of only those with an energy above a specified threshold, $\epsilon_\gamma^{\rm min} = 200\,{\rm keV}$. For photons above that threshold, the emission direction is sampled uniformly over 4π and a Lorentz boost is performed to express the emitted photon and the nuclear residue in the overall reference frame.

This procedure is iterated until the nuclear excitation energy falls below the specified minimum value $\epsilon_\gamma^{\min}$.

IV. ILLUSTRATIVE RESULTS

Here, we wish to illustrate the utility of single-event models like FREYA by presenting a number of correlation observables that could not be addressed with earlier codes that have tended to focus on more inclusive quantities. Obviously, the present preliminary version of FREYA involves a number of simplifying approximations and, consequently, the results cannot be expected to be numerically accurate. Certainly, for the most common observables, such as average multiplicities and spectra, the most reliable results can undoubtedly be obtained from the well-tuned codes that have long been available. We expect that event simulation codes will, in due course, achieve a similar level of accuracy. Meanwhile, they may serve as useful supplements with which is will be possible to address more detailed observables on an approximate level.

While the main purpose here is to illustrate the kind of novel information that can be accessed with FREYA, we wish to first show a number of more familiar observables. Throughout we consider fission induced by thermal neutrons on ^{235}U and ^{239}Pu. Fission induced by higher-energy neutrons is not considered, because the possibility of prefission neutron emission (and the associated nth chance fission) has not yet been included.

A. Fission fragments

The most basic observable is perhaps the product mass distribution $P(A_p)$ that, by design, matches the fits to the observed data and thus need not be displayed.

We therefore start by considering the kinetic energies of the fission fragments. Figure 1 shows the combined kinetic energy of both fragments, $K_{\rm tot}$, as a function of the mass number of the heavy fragment, A_H, while Fig. 2 shows the kinetic energy of a single fragment as a function of its mass number A_f. These results exhibit the general observed features, though the detailed behavior is not yet expected to be accurate.

The figures show the mean values of the kinetic energies as well as the associated dispersions. A quick comparison of the two figures suggests that the variance of the total kinetic energy is generally larger than the sum of the variances of the individual kinetic energies. This striking feature is an elementary consequence of momentum conservation. Because the two fragments emerge with opposite momenta, the fluctuations in their kinetic energies are closely correlated. As a result, the sum of the variances of the two individual fragment energies, K_L and K_H, is significantly smaller than the variance in the combined fragment energy $K_{LH} = K_L + K_H$, namely $\sigma^2(K_L) + \sigma^2(K_H) = [1 - 2A_L A_H/A_0^2]\,\sigma^2(K_{LH})$. In particular, for a symmetric split, $A_L = A_H$, we have $\sigma(K_i) = \frac{1}{2}\sigma(K_{LH})$ hence $\sigma(K_{LH})^2 = 2[(\sigma(K_L)^2 + \sigma(K_H)^2]$.

While the total excitation of the emerging fragments is related to their total kinetic energy by energy conservation, its partition is less straightforward, depending both on the relative heat capacities (i.e., level densities) and the scission

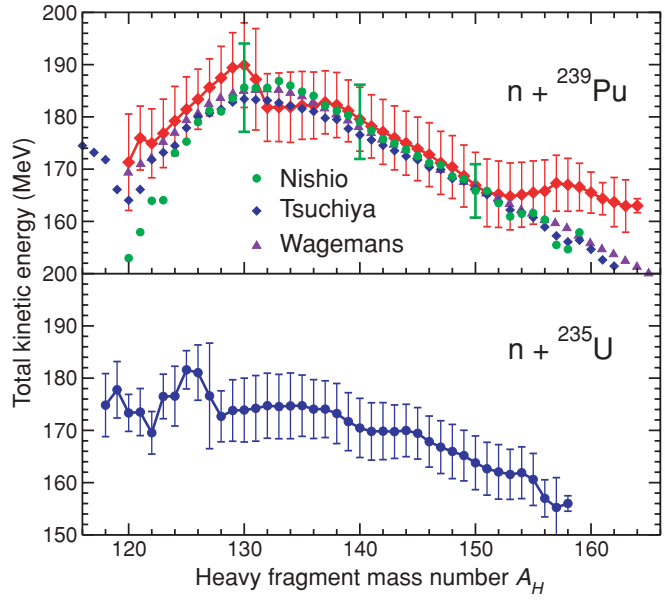

FIG. 1. (Color online) The mean total kinetic energy, $\overline{K}_{\rm tot}$, of the two fission fragments, and the associated dispersion (bars), as a function of the mass number of the heavy fragment, A_H, for 0.53 MeV n on ^{235}U (bottom) and ^{239}Pu (top). The data from Nishio [14] (with a few representative dispersions), Tsuchiya [15], and Wagemans [16] are shown. The dispersions reflect the width of the kinetic energy distribution and are not (experimental or theoretical) uncertainties.

fluctuations. Figure 3 shows the mean fragment excitation $\overline{E}_f^*$ together with the associated dispersion, as a function of the fragment mass number A_f. In the present model,

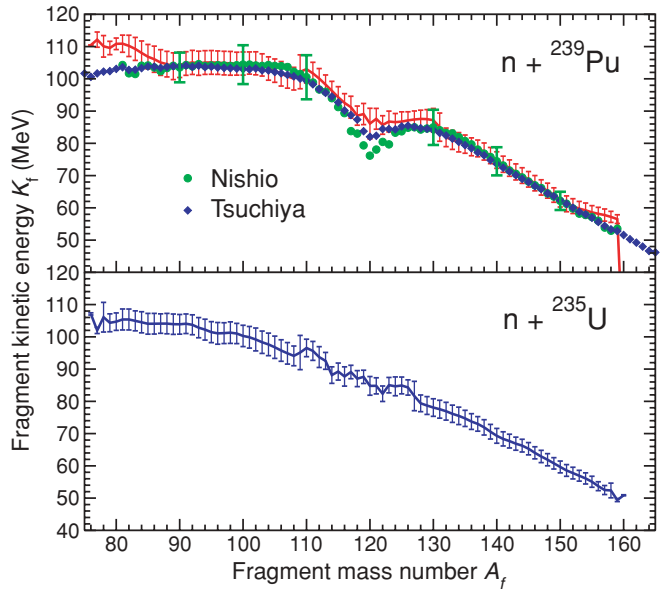

FIG. 2. (Color online) The mean kinetic energy of a single fragment and the associated dispersion (bars) as a function of its mass number A_f, for 0.53 MeV n on ^{235}U (bottom) and ^{239}Pu (top). Pu data from Nishio [14] and Tsuchiya [15] are shown.

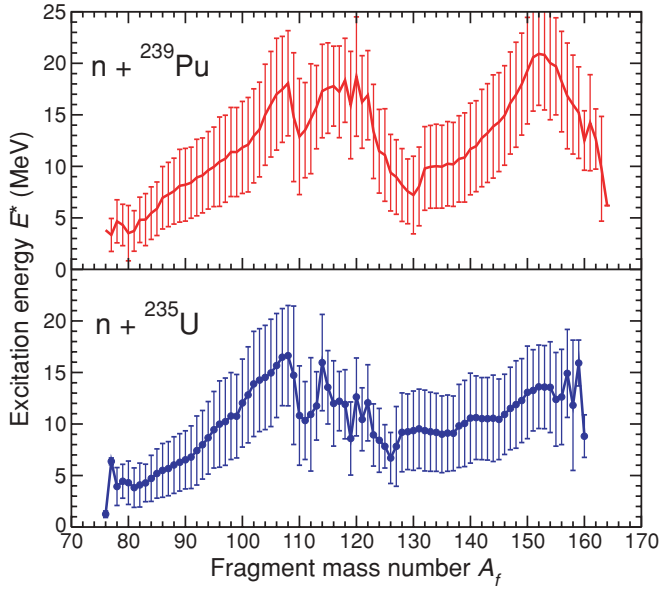

FIG. 3. (Color online) The mean excitation energy $\overline{E}^*$ (curves) of a fission fragment and the associated dispersion (bars), as a function of the mass number A_f for 0.53 MeV n on ^{235}U (bottom) and ^{239}Pu (top).

the division of the available energy between kinetic and excitation is sensitive to the degree of distortion of the scission prefragments, a property that in turn depends on the shell structure of the specific nuclides.

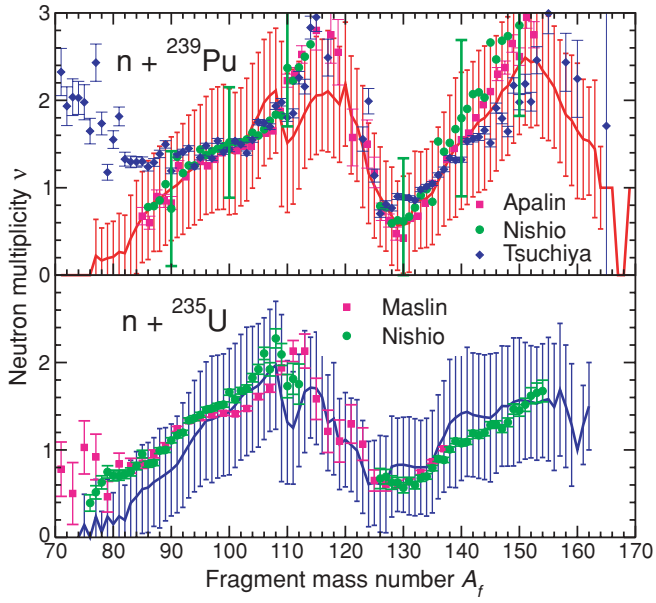

FIG. 4. (Color online) The mean number of neutrons (curve) resulting from fission fragment of a particular mass number A_f, with the associated dispersion indicated (bars), for 0.53 MeV n on ^{235}U (bottom) and ^{239}Pu (top). Data from Apalin [17], Maslin [18], Nishio [14,19], and Tsuchiya [15] are shown.

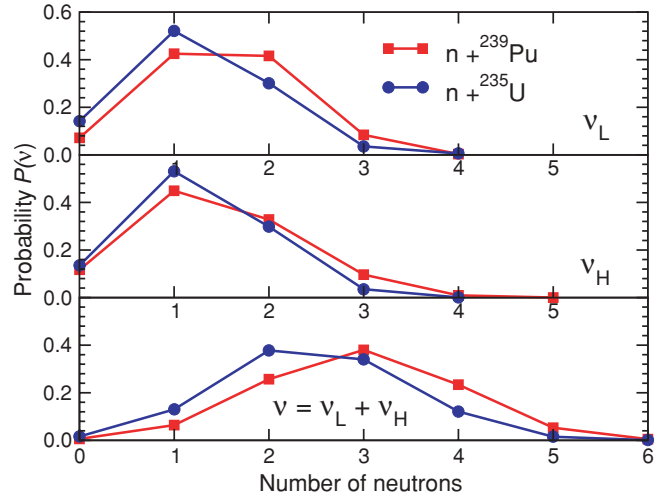

FIG. 5. (Color online) Multiplicity distributions for neutrons emitted by the light (top), the heavy (middle), or either (bottom) fragment resulting from thermal-neutron induced fission of ^{235}U (circles, blue) and ^{239}Pu (squares, red).

B. Neutron multiplicities

The fission fragment excitation energies $E^*(A_f)$ (see Fig. 3) largely determine the multiplicities of evaporated neutrons $\nu(A_f)$. This correspondance is clearly seen in Fig. 4, which shows the mean neutron multiplicity $\overline{\nu}(A_f)$ and the associated dispersion $\sigma_\nu(A_f)$. We note that the observed sawtooth shape is roughly reproduced, though the detailed behavior is not completely satisfactory.

The overall neutron multiplicity distribution $P(\nu)$ is shown in Fig. 5. This figure also shows the separate multiplicity distributions $P(\nu_L)$ and $P(\nu_H)$ for the number of neutrons ν_L and ν_H that were emitted by the light or the heavy fragment, respectively, a quantity that is difficult to obtain experimentally. The associated average multiplicities are shown in Table I ($\overline{\nu}_L \equiv \langle \nu_L \rangle$, etc.).

We note that the light fragment tends to emit more than its "fair share" of neutrons, a reflection of the fact that the excitation energy is not divided solely in proportion to mass. Furthermore, as the correlation coefficient C_{LH} shows, there is a slight anticorrelation between ν_L and ν_H. This feature is presumably a result of the anticorrelation between the excitations of the two partner fragments caused by the thermal fluctuations of the heat partition at scission.

Finally, Fig. 6 shows how the average total fragment kinetic energy of the fission products and their excitation depend on

TABLE I. The mean number of neutrons emitted from either the light fragment, $\overline{\nu}_L$, the heavy fragment, $\overline{\nu}_H$, or either fragment, $\overline{\nu} = \overline{\nu}_L + \overline{\nu}_H$, in fission events induced by thermal neutrons on ^{235}U and ^{239}Pu. Also shown is the correlation coefficient $C_{LH} \equiv \sigma(\nu_L, \nu_H)/[\sigma(\nu_L)\sigma(\nu_H)]$.

	$\overline{\nu}_L$	$\overline{\nu}_H$	$\overline{\nu}$	C_{LH}
n + ^{239}Pu	1.53	1.43	2.96	−0.19
n + ^{235}U	1.23	1.23	2.47	−0.12

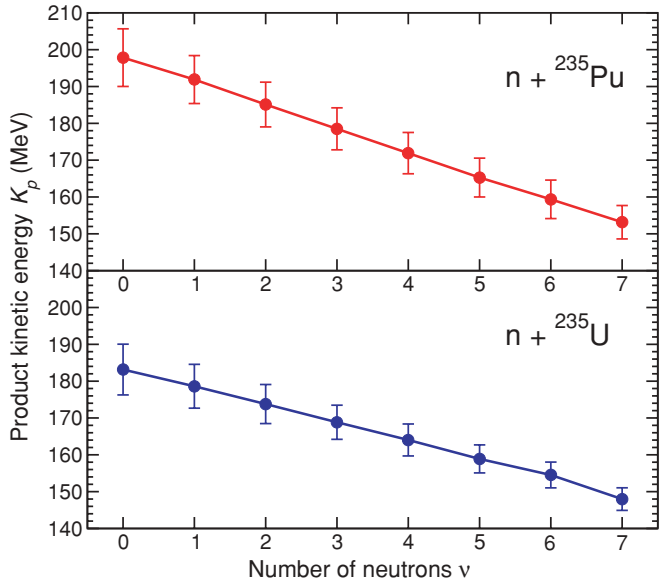

FIG. 6. (Color online) The mean total kinetic of energy the fission products together with the associated dispersions (bars), as a function of the neutron multiplicity in the event, for 0.53 MeV n on ^{235}U (bottom) and ^{239}Pu (top).

the number of evaporated neutrons ν. The decreasing character of the curves is easily understood because larger neutron multiplicities tend to arise from higher fragment excitations, which occurs in events with lower kinetic energies.

C. Neutron energies

We now turn to the kinetic energies of the evaporated neutrons. Figure 7 shows the fragment-mass dependence of

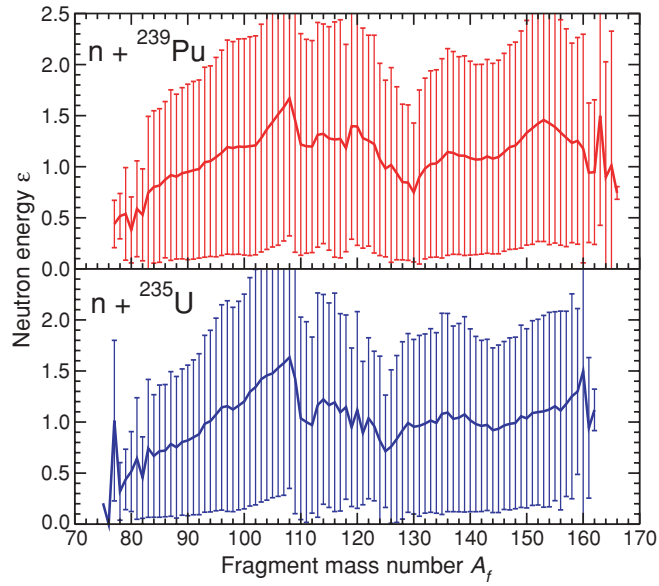

FIG. 7. (Color online) The mean neutron energy $\bar{\epsilon}_n$ (curves) together with its dispersion (bars) as a function of fragment mass A_f for 0.53 MeV n on ^{235}U (bottom) and ^{239}Pu (top).

TABLE II. The mean kinetic energy $\bar{\epsilon}_n$ (MeV) of the neutrons evaporated from the light fragment (L), the heavy fragment (H), or from either one ($L + H$), as a function of the respective multiplicity ν_L, ν_H, or ν, in fission events induced by thermal neutrons on ^{235}U (bottom) and ^{239}Pu (top).

	ν	All	1	2	3	4	5	6	7
	L	2.30	2.38	2.30	2.19	2.02			
Pu	H	1.64	1.70	1.64	1.58	1.50	1.34	1.17	
	$L + H$	1.98	2.10	2.09	2.01	1.93	1.82	1.74	1.68
	L	2.18	2.22	2.17	2.05	1.85			
U	H	1.50	1.56	1.46	1.39	1.24			
	$L + H$	1.84	1.85	1.88	1.84	1.79	1.73	1.67	1.55

the mean kinetic energy with respect to the frame of the emitting nucleus together with the associated dispersion of the kinetic-energy distribution.

The neutron spectra depend somewhat on the number of neutrons emitted. This is summarized in Table II, which shows the mean kinetic energy of neutrons emitted from the light fragment, the heavy fragment, or from either one as a function of the respective neutron multiplicities ν_L, ν_H, and $\nu = \nu_L + \nu_H$.

The mean energies, as seen in the laboratory, as well as the associated dispersions, are displayed in Fig. 8 for the three neutron categories. In each case, there is an overall

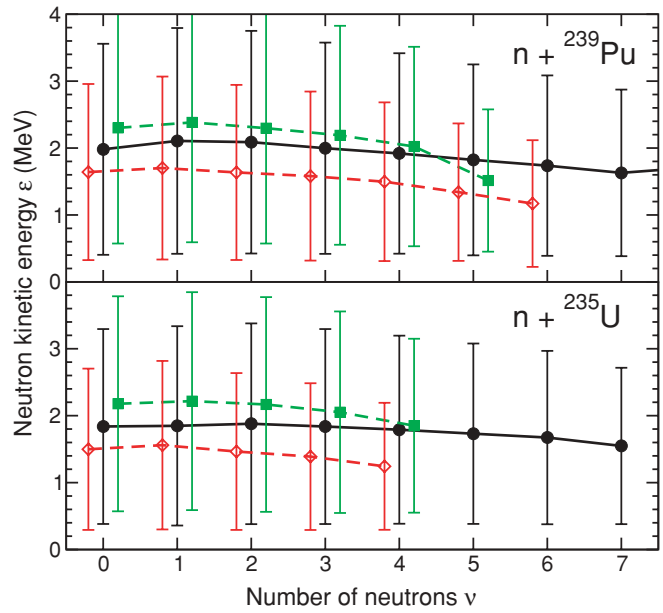

FIG. 8. (Color online) The mean kinetic energy and the associated dispersions of all the neutrons emitted in fission events with a specified total neutron multiplicity ν, induced by thermal neutrons on ^{239}Pu and ^{235}U (solid curve, black dots), as well as the mean kinetic energy and the associated dispersions of all the neutrons emitted from the light fragment as a function of the corresponding multiplicity ν_L (dashed curve, green squares) and the mean kinetic energy and the associated dispersions of all the neutrons emitted from the heavy fragment as a function of the corresponding multiplicity ν_H (dashed curve, red diamonds).

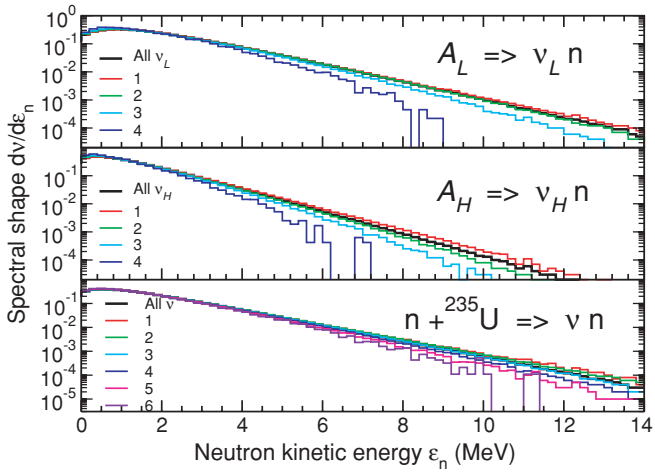

FIG. 9. (Color online) The spectral shape of neutrons evaporated from the light (top), the heavy (middle), or either (bottom) fragment for specified values of the respective multiplicity ν_L, ν_H, or ν, in fission induced by thermal neutrons on ^{235}U.

relatively modest decrease of the average neutron energy (and a corresponding narrowing of the distribution) as the neutron multiplicity is increased. This feature would be expected since the available energy must be shared among more neutrons.

The full multiplicity-gated spectral shapes are shown in Figs. 9 (for U) and 10 (for Pu). It is apparent that the spectra become progressively softer at higher multiplicities. This type of information is not provided by the standard models and is therefore novel.

D. Neutron-neutron angular correlations

The event-by-event calculation makes it straightforward extract the angular correlation between two evaporated neutrons, an observable that has long been of experimental interest (see, for example, Refs. [20–22] and references therein) but that cannot be addressed with the standard models of fission.

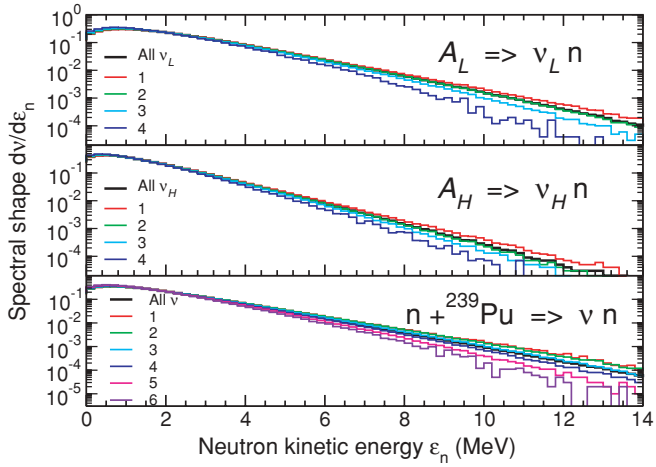

FIG. 10. (Color online) Similar to Fig. 9 but for n + ^{239}Pu.

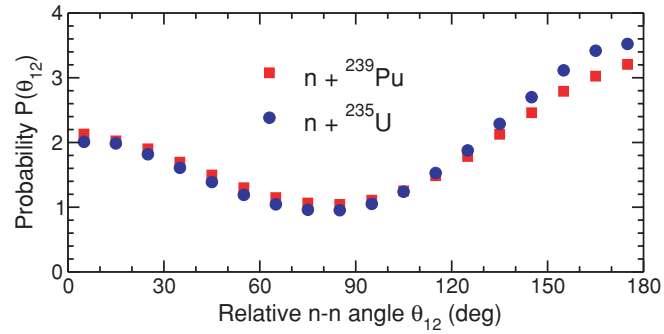

FIG. 11. (Color online) The angular correlation between two evaporated neutrons for 0.53 MeV n on ^{235}U and ^{239}Pu, considering only neutrons with a kinetic energy above 1 MeV.

Figure 11 shows this quantity for the neutrons resulting from fission induced by thermal neutrons on ^{235}U and ^{239}Pu. The analysis shown included only neutrons with kinetic energy above a threshold of 1 MeV. The results look qualitatively similar for other threshold energies, with the angular modulation growing somewhat more pronounced as the threshold is raised (while the counting statistics is correspondingly reduced).

We see that the neutrons tend to be either forward or backward correlated. The backward correlation appears to be somewhat favored, as would be expected from the relatively small but negative value of the multiplicity correlation coefficient C_{LH} shown in Table I.

E. Neutron-photon correlations

The final illustration is relevant for the correlation between the neutron and photon multiplicities. Figure 12 shows

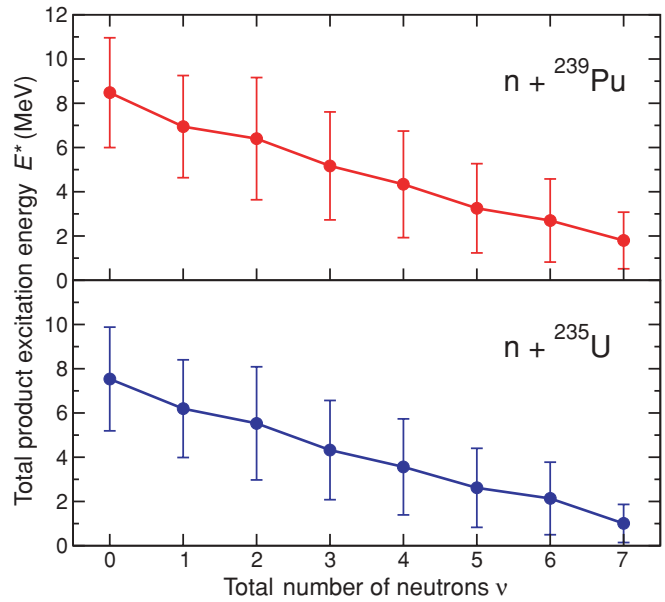

FIG. 12. (Color online) The mean total excitation energy of the two fission products, together with the associated dispersions (bars), as a function of the neutron multiplicity in the event, for 0.53 MeV n on ^{235}U (bottom) and ^{239}Pu (top).

TABLE III. The mean neutron multiplicity $\overline{\nu} = \langle \nu \rangle$ and the associated dispersion σ_ν, the mean photon multiplicity $\overline{\mu} = \langle \mu \rangle$ and the associated dispersion σ_μ, and the neutron-photon multiplicity covariance $\sigma_{\nu\mu} \equiv \langle \nu\mu \rangle - \overline{\nu}\,\overline{\mu}$ together with the corresponding correlation coefficient $C_{n\gamma} = \sigma_{\nu\mu}/[\sigma_\nu \sigma_\mu]$, for photons with transition energies above 200 keV.

	$\overline{\nu}$	σ_ν	$\overline{\mu}$	σ_μ	$\sigma_{\nu\mu}$	$C_{n\gamma}$
n + ^{239}Pu	2.97	1.03	5.67	2.49	−0.84	−0.33
n + ^{235}U	2.49	0.96	5.40	2.40	−0.79	−0.34

the combined excitation left in the two product nuclei as a function of the total number of evaporated neutrons. When more neutrons are emitted the residual product nuclei are less excited. This feature appears to be reasonable because a larger-than-average number of neutrons is likely to have used up a larger-than-average portion of the total available excitation energy, thus leaving a less-than-average amount of residual excitation.

Because the average number of photons emitted from a given product increases monotonically with excitation, the results in Fig. 12 provide a qualitative indication of the correlation between the number of neutrons evaporated and the number of photons emitted during the further de-excitation of the product nuclei. Our simulations thus suggest that the two multiplicities are anticorrelated: the more neutrons the fewer photons.

This qualitative expectation is borne out by Table III, which summarizes the result of including the actual photon multiplicity μ into the analysis. The covariance between ν and μ is indeed negative and the corresponding correlation coefficient is about minus one-third, suggesting a fairly significant degree of anticorrelation.

V. CONCLUDING REMARKS

Over the past few years, experimental capabilities have improved dramatically while the practical applications of fission have broadened significantly. As a consequence, there has been an growing need for calculations of increasingly complex observables that are beyond the scope of the traditional models employed in the field.

To meet this need, we have developed a new calculational framework, `FREYA`, which can generate large samples of individual fission events. From those it is then possible to extract any specific correlation observable of interest, without the need for further approximation. In developing `FREYA`, we have sought to make the numerics sufficiently fast to facilitate use of the code as a practical calculational tool. (Thus, on a MacBook laptop computer, it takes about 12 s to generate one million events.)

Our early emphasis has been on creating a working code that can produce samples of reasonably realistic fission events and form a convenient basis for gradual refinements. (Its simple modular structure should facilitate such further developments.) Consequently, the present version is still rather rough and cannot compete for quantative accuracy with established models without suitable *ad hoc* parameter adjustments (see Ref. [3]). Even so, the model has already proven to be capable of making interesting predictions for correlations of interest in variety of contexts and we foresee an increased number of applications.

ACKNOWLEDGMENTS

We wish to acknowledge helpful discussions with D. A. Brown, D. Gogny, E. Ormand, P. Möller, E. B. Norman, J. Pruet, W. J. Swiatecki, P. Talou, and W. Younes. This work was supported by the Director, Office of Energy Research, Office of High Energy and Nuclear Physics, Nuclear Physics Division of the US Department of Energy under Contract Nos. DE-AC02-05CH11231 (JR) and DE-AC52-07NA27344 (RV) and by the National Science Foundation, Grant NSF PHY-0555660 (RV).

APPENDIX A: LIQUID-DROP MODEL

For simplicity, we use here the liquid-drop model [23] for the macroscopic part of the nuclear binding energy. Accordingly, the surface and Coulomb energy of a spherical nucleus are given by

$$E_S^0({}^A Z) = a_2 A^{2/3}\left[1 - \kappa\left(\frac{N-Z}{2A}\right)^2\right] \tag{A1}$$

$$E_C^0({}^A Z) = c_3 \frac{Z^2}{A^{1/3}} \tag{A2}$$

with the Lysekil parameter values: $a_2 = 17.9439$ MeV, $\kappa = 1.7826$, $c_3 = \frac{3}{5}e^2/r_0 = 0.7053$ MeV [24].

The distortion energies of the prefragments at scission are based on the shape dependence of the surface and Coulomb energies of macroscopic prolate nuclei [6]

$$E_S(\varepsilon) = E_C^0 B_S(\varepsilon) \approx E_S^0\left[1 + \tfrac{8}{45}\varepsilon^2\right] \tag{A3}$$

$$E_C(\varepsilon) = E_C^0 B_S(\varepsilon) \approx E_C^0\left[1 - \tfrac{4}{45}\varepsilon^2\right]. \tag{A4}$$

APPENDIX B: LEVEL DENSITIES

The relationship between the nuclear excitation energy E^* and the nuclear temperature T is generally somewhat complicated. For the time being, we simply use the familiar approximation $T = \sqrt{\varepsilon^*/a}$, where $\varepsilon^* = E^* - \delta E_{\rm def}$ is the statistical part of the excitation energy (the "heat"). For a given nucleus (Z_i, A_i) the level-density parameter a_i is taken from Ref. [25],

$$a_i(E^*) = \frac{A_i}{e_0}\left[1 + \frac{\delta W_i}{U_i}(1 - \mathrm{e}^{-\gamma U_i})\right], \quad U_i \equiv E^* - \Delta_i \tag{B1}$$

with $e_0 = 7.25$ MeV and $\gamma = 0.05$. Here $\tilde{a}_i = A_i/e_0$ is the asymptotic level-density parameter whose parameter e_0

depends slightly on the specific value used for the damping coefficient γ. The shell correction energies $\{\delta W_i\}$ and the pairing energies $\{\Delta_i\}$ are those calculated by Koura *et al.* [10] for nuclei with $20 \leqslant Z_i \leqslant 92$. We note that $a_i(E^* \approx \Delta) \approx \tilde{a}_i\{1 + \delta_i\gamma[1 - \frac{1}{2}(E^* - \Delta_i)]\}$ is regular. Furthermore, $a_i(E^* = 0) \approx \tilde{a}_i[1 + \gamma\delta W_i]$ when $\gamma U_i \ll 1$, which is most often the case. Finally, as E^* is increased we have $a_i(E^*) \to \tilde{a}_i[1 + \delta W_i/E^*] \to \tilde{a}_i \equiv A_i/e_0$.

APPENDIX C: SPECTRAL SAMPLING

It is possible to devise a fast algorithm for sampling the spectral distribution (11) for the evaporated neutron, $dN/d\epsilon \propto \epsilon\, \mathrm{e}^{-\epsilon/T}$. It is based on the observation that the function $x\mathrm{e}^{-x}$ is a (normalized) Poisson distribution of order 2. Hence it can be expressed as the convolution of two (normalized) exponentials (each of which is a Poisson distribution of order 1), $P_2 = P_1 * P_1$ with $P_1(x) \equiv \mathrm{e}^{-x}$,

$$x\mathrm{e}^{-x} = \int_0^\infty dx_1 \int_0^\infty dx_2 \delta(x_1 + x_2 - x)\, \mathrm{e}^{-x_1}\mathrm{e}^{-x_2}. \quad \text{(C1)}$$

This is a special case of the general feature of Poisson distributions, $P_{n+m} = P_n * P_m$.

We may therefore obtain a sampled value of the kinetic energy ϵ as the sum of two energies, ϵ_1 and ϵ_2, that have each been sampled from a usual exponential distribution $\propto \mathrm{e}^{-\epsilon_i/T}$. Because the sampling from an exponential distribution $p(x) = \mathrm{e}^{-x}$ is readily accomplished by sampling a random number η that is uniformly distributed on the interval $(0, 1]$ and then taking the negative of its logarithm, $x = -\ln\eta$, the relative neutron kinetic energy is

$$\epsilon_\mathrm{n} = \epsilon_1 + \epsilon_2 = -[\ln\eta_1 + \ln\eta_2]T_f^{\max}, \quad \eta_i \in (0, 1] \quad \text{(C2)}$$

where the two numbers η_i have been sampled from $(0, 1]$. Because both mean values and variances are additive under convolution and each exponential distribution yields $\langle\epsilon_i\rangle = T$ and $\sigma^2(\epsilon_i) = T^2$, the resulting relative kinetic energy ϵ_n has the mean value $\langle\epsilon_\mathrm{n}\rangle = 2T_f^{\max}$ and the variance $\sigma^2(\epsilon_\mathrm{n}) = 2(T_f^{\max})^2$, for a fixed value of $T_f^{\max}$.

The energy spectrum of the postevaporation photons can be sampled rapidly in an analogous manner, Because the corresponding spectral shape, $dN/d\epsilon \propto \epsilon^2\mathrm{e}^{-\epsilon/T_f}$, is (proportional to) a Poisson distribution of order 3, so

$$\varepsilon_\gamma = -[\ln\eta_1 + \ln\eta_2 + \ln\eta_3]T_f, \quad \eta_i \in (0, 1]. \quad \text{(C3)}$$

It also follows that the mean value is $\langle\epsilon_\gamma\rangle = 3T_f$ and the variance is $\sigma^2(\epsilon_\gamma) = 3T_f^2$, for a fixed value of T_f.

APPENDIX D: LORENTZ BOOST

We describe here the Lorentz boost required to express the motion of an ejectile and the corresponding daughter nucleus in the adopted reference frame.

The boost velocity is that of the mother nucleus, $\boldsymbol{V}_i = \boldsymbol{P}_i/E_i$, where $\boldsymbol{P}_i$ is the momentum of the mother nucleus and E_i is its total energy, $E_i^2 = (M_i^*)^2 + P_i^2$. To perform the Lorentz boost, we first note that the component of the ejectile momentum parallel to the boost velocity is $p_\mathrm{n}^\parallel = \boldsymbol{p}_\mathrm{n} \cdot \hat{\mathbf{v}}$, where $\hat{\mathbf{v}} \equiv \boldsymbol{V}_i/V_i$ is the unit vector in the direction of $\boldsymbol{V}_i$. The component transverse to $\boldsymbol{V}_i$ is then $\boldsymbol{p}_\mathrm{n}^\perp = \boldsymbol{p}_\mathrm{n} - p_\mathrm{n}^\parallel\hat{\mathbf{v}}$ and this component is unaffected by the boost, $\tilde{\boldsymbol{p}}_\mathrm{n}^\perp = \boldsymbol{p}_\mathrm{n}^\perp$. The parallel component of the ejectile momentum and its energy transform as follows,

$$\tilde{p}_\mathrm{n}^\parallel = \gamma(p_\mathrm{n}^\parallel + E_\mathrm{n}V_i), \quad \tilde{E}_\mathrm{n} = \gamma(E_\mathrm{n} + \boldsymbol{p}_\mathrm{n} \cdot \boldsymbol{V}_i), \quad \text{(D1)}$$

where $\gamma^2 = 1/(1 - V_i^2)$ and $E_\mathrm{n}^2 = m_\mathrm{n}^2 + p^2$. Thus the boosted ejectile momentum is

$$\tilde{\boldsymbol{p}}_\mathrm{n} = \left[\gamma E_\mathrm{n} + \frac{\gamma - 1}{V_i^2}\, \boldsymbol{p}_\mathrm{n} \cdot \boldsymbol{V}_i\right]\boldsymbol{V}_i + \boldsymbol{p}_\mathrm{n} \quad \text{(D2)}$$

while the boosted value of the recoil momentum is obtained by reversing the direction of $\boldsymbol{p}$,

$$\tilde{\boldsymbol{P}}_f = \left[\gamma E_f - \frac{\gamma - 1}{V_i^2}\, \boldsymbol{p}_\mathrm{n} \cdot \boldsymbol{V}_i\right]\boldsymbol{V}_i - \boldsymbol{p}_\mathrm{n} \quad \text{(D3)}$$

with E_f being the total energy of the daughter, $E_f^2 = (M_f^*)^2 + p^2$.

[1] D. G. Madland and J. R. Nix, Nucl. Sci. Eng. **81**, 213 (1982).
[2] S. Lemaire, P. Talou, T. Kawano, M. B. Chadwick, and D. G. Madland, Phys. Rev. C **72**, 024601 (2005).
[3] R. Vogt, J. Randrup, J. Pruet, and W. Younes (submitted to Phys. Rev. C), arXiv:0907.5045 [nucl-th].
[4] W. Younes, J. A. Becker, L. A. Bernstein, P. E. Garrett, C. A. McGrath, D. P. McNabb, R. O. Nelson, G. D. Johns, W. S. Wilburn, and D. M. Drake, Phys. Rev. C **64**, 054613 (2001).
[5] W. Reisdorf, J. P. Unik, H. C. Griffin, and L. E. Glendenin, Nucl. Phys. **A177**, 337 (1971).
[6] R. W. Hasse and W. D. Myers, *Geometrical Relationships of Macroscopic Nuclear Physics* (Springer-Verlag, New York, 1988).
[7] S. Cohen and W. J. Swiatecki, Ann. Phys. **19**, 67 (1962).
[8] G. Audi and A. H. Wapstra, Nucl. Phys. **A595**, 409 (1995).
[9] P. Möller, J. R. Nix, W. D. Myers, and W. J. Swiatecki, At. Data Nucl. Data Tables **59**, 185 (1995).
[10] H. Koura, M. Uno, T. Tachibana, and M. Yamada, Nucl. Phys. **A674**, 47 (2000).
[11] V. F. Weisskopf, Phys. Rev. **52**, 295 (1937).
[12] J. M. Blatt and V. F. Weisskopf, *Theoretical Nuclear Physics* (John Wiley & Sons, Inc., New York, 1952), p. 365.
[13] S. Lemaire, P. Talou, T. Kawano, M. B. Chadwick, and D. G. Madland, Phys. Rev. C **73**, 014602 (2006).
[14] K. Nishio, Y. Nakagome, I. Kanno, and I. Kimura, J. Nucl. Sci. Technol. **32**, 404 (1995).
[15] C. Tsuchiya, Y. Nakagome, H. Yamana, H. Moriyama, K. Nishio, I. Kanno, K. Shin, and I. Kimura, J. Nucl. Sci. Technol. **37**, 941 (2000).
[16] C. Wagemans, E. Allaert, A. Deruytter, R. Barthélémy, and P. Schillebeeckx, Phys. Rev. C **30**, 218 (1984).
[17] V. F. Apalin, Yu. N. Gritsyuk, I. E. Kutikov, V. I. Lebedev, and L. A. Mikaelian, Nucl. Phys. **A71**, 553 (1965).
[18] E. E. Maslin and A. L. Rodgers, Phys. Rev. **164**, 1520 (1967).

[19] K. Nishio, Y. Nakagome, H. Yamamoto, and I. Kimura, Nucl. Phys. **A632**, 540 (1998).
[20] S. DeBenedetti, J. E. Francis, Jr., W. M. Preston, and T. W. Bonner, Phys. Rev. **74**, 1645 (1948).
[21] C. B. Franklyn, C. Hofmeyer, and D. W. Mingay, Phys. Lett. **B78**, 564 (1978).
[22] A. M. Gagarski *et al.*, Bull. Russ. Acad. Sci. Phys., **72**, 773 (2008).
[23] W. D. Myers and W. J. Swiatecki, Nucl. Phys. **81**, 1 (1966).
[24] W. D. Myers and W. J. Swiatecki, Ark. Fys. **36**, 343 (1967).
[25] T. Kawano, S. Chiba, and H. Koura, J. Nucl. Sci. Technol. **43**, 1 (2006).